Numerical investigation of droplet evaporation in high-pressure dual-fuel conditions using a tabulated real-fluid model

Hesham Gaballa*, Sajad Jafari, Chaouki Habchi*, Jean-Charles de Hemptinne
IFP Energies Nouvelles, Institut Carnot Transports Energies, 1 et 4 Avenue de Bois-Préau, 92852 Rueil-Malmaison, France

Abstract

The substitution of diesel by cleaner renewable fuels such as short-chain alcohols in dual-fuel internal combustion engines is considered an attractive solution to reduce the pollutant emissions from internal combustion engines. In this context, two-phase flow models for multi-component mixtures considering the real-fluid thermodynamics are required for further understanding the evaporation and mixing processes in transcritical conditions. The present study proposes an efficient real-fluid model (RFM) based on a two-phase, fully compressible four-equation model under mechanical and thermal equilibrium assumptions with a diffused interface and closed by a thermodynamic equilibrium tabulation approach. Compared to previous research limited to binary mixtures tabulation, the proposed pre-tabulation approach can further handle ternary mixtures using a thermodynamic table that has been coupled to the CONVERGE CFD solver. The newly developed RFM model has been applied to investigate the evaporation of an n-dodecane droplet in a mixed ambient (methanol and nitrogen) relevant to dual-fuel configuration compared to pure nitrogen ambient. The four equation model is closed by a tabulated Cubic Plus Association (CPA) and Peng-Robinson (PR) equations of state for the droplet evaporation in a mixed and single component ambient, respectively. Numerical predictions show that the n-dodecane droplet lifetime decreases monotonically with increasing the methanol ambient concentration under the considered transcritical conditions. The performed thermodynamic analysis demonstrates that the droplet follows a different thermodynamic path as a function of the methanol ambient concentration. The different mechanisms contributing to the droplet lifetime behavior under varying ambient conditions are discussed.

*Corresponding author, Email: hesham.gaballa@ifpen.fr (H.G.); chawki.habchi@ifpen.fr (C.H.)

Keywords: droplet evaporation; real-fluid model; two-phase flow; thermodynamic tabulation; vapor-liquid equilibrium; ternary mixture;

1 Introduction

The recent strict emissions legislation in Europe [22] or the US [16] poses new challenges on the continuous use of internal combustion engines (ICE), owing to their carbon dioxide (CO_2) and soot emissions, which respectively accelerates climate change and leads to severe health problems [49]. Dual-fuel internal combustion engines (DFICE) using alternative renewable fuels are among the promising solutions for reducing emissions from fossil fuel combustion. Indeed, dual-fuel engines are employed in various applications such as cargo ships, heavy-duty trucks, and marine engines [29], where electrification is not yet considered a feasible solution to the emissions problem. In dual-fuel engines, primary fuels such as natural gas or short-chain alcohols (methanol/ethanol) are employed, along with a moderate amount of pilot diesel fuel to ignite the premixed air-primary fuel mixture. A review of the different primary fuel injection strategies in dual-fuel engines can be found in [54]. Recent experimental studies [34, 13, 40] have demonstrated the potential of employing primary fuels such as methanol or ethanol in DFICE to reduce the soot and nitrogen oxides (NOx) emissions. These fuels offer several advantages, including being renewable, lower cost, and can be produced from biomass. Despite the aforementioned advantages, the effective design of the fuel injection equipment (FIE) for DFICE is a challenging task and a key priority for the further development of these engines. To this goal, fuel injection and mixing need to be further understood. In this work, the evaporation and mixing of spray fuel droplets relevant to the dual-fuel configuration are investigated due to their direct impact on the combustion process and resulting emissions.

Extensive numerical and experimental investigations can be found in the literature regarding single or multi-component droplet evaporation of particular interest to those at high ambient pressures more relevant to realistic operating conditions. The droplet support method is one of the experimental techniques that has been widely used to study isolated droplet evaporation [38, 17]. However, a well-known problem of the support fiber method is the increase of the droplet evaporation rate due to the heat conduction through the support fiber when employing large fiber diameters [7, 8, 14]. Besides, the suspended droplet technique cannot be employed for supercritical fluid states, as the approach requires surface tension to attach the droplet onto the fiber. To circumvent these issues, Crua et al. [11] employed a fuel injector to generate droplets of normal alkanes (n-heptane, n-dodecane, n-hexadecane) in transcritical conditions, where the ambient temperature and pressure are higher than the critical point of the injected fuel. They performed a high-resolution microscopic visualization of individual droplets tracked at the end of the fuel injection event until they were completely vaporized. In addition, they proposed a transition criterion from the classical subcritical phase change to diffusive mixing regime.

On the numerical side, various investigations of droplet evaporation can be found in the literature. These investigations included detailed numerical models solving the Navier-

Stokes (NS) equations to simpler models employing correlations to predict the heat and mass transfer processes. Schlottke et al. [48] studied the evaporation of deformed droplets based on the Volume of Fluid (VOF) method along with solving the incompressible NS equations, and the evaporation rate was computed based on the mass fraction gradient at the interface [47]. Strotos et al. [51] presented a model that solves the NS equations, energy conservation and species transport equations, and the VOF methodology to capture the liquid-gas interface. The simulated ambient temperatures range from 0.56 to 1.2 fuel's critical temperature under atmospheric pressure conditions. A local evaporation rate model was used based on the local vapor concentration gradient at the liquid-gas interface and assuming local thermodynamic equilibrium. Extensive reviews of single or multi-component droplet evaporation models can be found in [46, 5, 37]. The research mentioned above has mainly focused on single or multi-component droplet evaporation in a non-condensable ambient (usually consisting of a single component), but in the present work, the ambient is considered as bi-component, including methanol and nitrogen, which is relevant to the dual-fuel strategy.

Regarding the evaporation modeling under elevated ambient pressures, many effects that are assumed negligible at low, moderate ambient pressures becomes important such as the solubility of the ambient gas in the liquid phase, non-ideal transport and thermodynamic properties, the transient character of both the liquid and gas phases, and the real gas effect on the vapor-liquid equilibrium (VLE) condition at the droplet interface [25, 27]. Jia and Gogos [26] have investigated the effect of the solubility of the ambient gas on the evaporation of n-hexane droplets. It was found that at ambient pressures lower than the critical point of the fuel, the droplet lifetime predicted with or without the ambient gas solubility agrees. However, as the ambient pressure exceeds the fuel's critical point, neglecting the ambient gas solubility leads to underestimating the droplet lifetime. Ebrahimian and Habchi [14] proposed an evaporation model for multi-component hydrocarbon droplets, where they demonstrated that at high ambient pressures, the mixture's non-ideality becomes significant, and the employment of real-gas equation of state (EoS) is needed. Accordingly, a real-fluid EoS is essential for accurate modeling of the fluid properties at such conditions. The application of droplet evaporation models from the literature at high-pressure conditions in dual-fuel configurations could be questioned. Indeed, the evaporation models predict the heat and mass transfer processes using correlations, which may require further adjustments to consider the interaction and mixing between the pilot and primary fuels in dual-fuel engines, which subsequently affects the heat transfer and vaporization rates. Therefore, it is highly desirable to have computational fluid dynamics (CFD) software capable of performing highly resolved numerical simulations for dual-fuel conditions, considering the real-fluid thermodynamics, for further understanding of the interaction between the different fuels involved. The current work aims at providing such simulation tool, which after validation, could also offer an alternative for the cases that

experimental techniques are not available.

In addition, the multi-component two-phase flow involved in such DFICE may exhibit different thermodynamic regimes based on the local pressure, temperature, and species composition compared to the mixture's critical point. Indeed, it cannot be determined from an *a priori* analysis whether the Spatio-temporal variation of the involved thermodynamic states are subcritical or supercritical during the entire fuel injection event. As a matter of fact, both subcritical and supercritical regimes may exist simultaneously, as discussed by [57, 35, 24]. Thereby, two-phase flow models that can handle such multi-component mixtures accurately and robustly are required for the further development of DFICE.

Several two-phase flow models have been proposed in the literature in the framework of the diffuse interface model (DIM) approach with transport equations ranging from four to seven based on the initial equilibrium assumptions [2, 44, 28, 20]. Among them, the four-equation model, which have been employed for cavitation and spray simulations [45, 21] owing to its high efficiency. The main challenge in such models is estimating the phase change source term for the classical subcritical phase change and the ability to transit to a supercritical single-phase mixing regime. Indeed, several researchers [57, 35, 9] have coupled the four-equation model with a VLE solver to estimate the phase change source term. However, it has been proved that the direct evaluation of VLE using a complex real-fluid EoS during the two-phase simulations run-time is computationally demanding [57, 60].

Accordingly, different solutions have been proposed in the literature to overcome the cumbersome and costly VLE solver. A first approach involves tabulating the VLE calculation before the CFD simulation, where an efficient interpolation of the stored quantities can be performed during the simulation based on the inputs provided by the flow solver. Several contributions based on pre-tabulated thermodynamic closures have been presented in the literature for two-phase flow simulations. Yi et al. [59] investigated n-dodecane droplets evaporation in transcritical conditions using a three-dimensional (3D) uniform tabulation approach based on the (VLE) solver developed by [60, 57]. Besides, Koukouvinis et al. [32] employed a tabulated thermodynamic approach based on ($log_{10}P-T$) tables to investigate the high pressure/temperature injection of n-dodecane in ECN spray A condition [1]. The aforementioned studies have proved that the pre-tabulation approach can be efficient and reliable, especially for complex cases, allowing for significant savings in terms of computational cost. However, the storage requirements for the tables may impose difficulty as the table dimensions are extended for multi-species systems. Recently, other alternatives to the pre-tabulation approach have also been proposed. Zhang and Yang [61] employed an in situ adaptive tabulation (ISAT) approach, where the table is constructed during the CFD simulation. Besides, Koukouvinis et al. [33] employed an artificial neural network (ANN) as a regression model for the thermodynamic properties. However, these

approaches are still under investigation and their efficiency for multi-component problems is not evaluated.

Therefore, the current work adopts an efficient pre-tabulation approach as initially proposed by Yi et al. [59], for binary systems. In this work, the tabulation approach is further developed to handle ternary mixtures as those encountered in dual-fuel engines, in contrast to the previous research limited to binary mixtures tabulation. More specifically, a four-dimensional (4D) thermodynamic table is generated for ternary mixture by the IFPEN-Carnot thermodynamic library, where the thermodynamic table is coupled to the CONVERGE CFD solver [43]. The newly developed real-fluid model (RFM) has been applied to investigate the evaporation of an n-dodecane droplet in a (methanol and nitrogen) bi-component ambient relevant to dual-fuel configuration compared to pure nitrogen ambient. The thermodynamic closure of the two-phase system is achieved using a tabulated Cubic Plus Association (CPA) [31] and Peng-Robinson (PR) [41] equations of state for the simulation of droplet evaporation in bi and single component ambient, respectively.

The main aim is to investigate the impact of the primary fuel (methanol) ambient concentration on the n-dodecane droplet evaporation characteristics under the transcritical ambient conditions of Crua et al. [11] experimental work. Moreover, to analyze the effect of the different solubilities of methanol and nitrogen on the droplet evaporation at the high ambient pressures considered. Besides, whether the evaporation and mixing processes take place at a subcritical or supercritical thermodynamic regime will also be investigated.

This paper is organized as follows. Section 2 describes the RFM model, including the set of transport equations and the new thermodynamic equilibrium tabulation approach for ternary systems. Section 3 presents a description of the simulated test cases, the employed numerical setup, and qualitative validation of the reference case with the experiments of [11]. Section 4 presents the results of droplet evaporation in mixed ambient under the considered ambient conditions. Finally, the conclusions are summarized in Section 5.

2 The real-fluid model (RFM) description

2.1 Governing equations

The diffused interface two-phase flow model adopted in the current study is a four equation model that is fully compressible and considers multi-component in both phases under the assumptions of thermal and mechanical equilibrium. The set of governing equations as employed in the CONVERGE CFD solver [43] are presented through Equations (2.1-2.4), including the density transport equation, mixture momentum equation, mixture specific

internal energy equation, and species transport equation, respectively.

$$\frac{\partial \rho}{\partial t} + \frac{\partial \rho u_i}{\partial x_i} = 0 \tag{2.1}$$

$$\frac{\partial \rho u_i}{\partial t} + \frac{\partial \rho u_i u_j}{\partial x_j} = -\frac{\partial P}{\partial x_i} + \frac{\partial \tau_{ij}}{\partial x_j} \tag{2.2}$$

$$\frac{\partial \rho e}{\partial t} + \frac{\partial \rho e u_j}{\partial x_j} = -P\frac{\partial u_j}{\partial x_j} + \tau_{ij}\frac{\partial u_i}{\partial x_j} + \frac{\partial}{\partial x_j}\left(\lambda \frac{\partial T}{\partial x_j}\right) + \frac{\partial}{\partial x_j}\left(\rho \sum_k D_{km} h_k \frac{\partial Y_k}{\partial x_j}\right) \tag{2.3}$$

$$\frac{\partial \rho Y_k}{\partial t} + \frac{\partial \rho Y_k u_j}{\partial x_j} = \frac{\partial}{\partial x_j}\left(\rho D_{km} \frac{\partial Y_k}{\partial x_j}\right) \tag{2.4}$$

where τ_{ij} corresponds to the viscous stress tensor ($\tau_{ij} = \mu(\partial u_i/\partial x_j + \partial u_j/\partial x_i) - \frac{2}{3}\mu(\partial u_k/\partial x_k \delta_{ij})$. (ρ, u_i, P, T, e) are the mixture's density, velocity, pressure, temperature, and specific internal energy, respectively. (Y_k, h_k) are the mass fraction and specific enthalpy of the individual species k, respectively. (λ) and (μ) are the thermal conductivity and dynamic viscosity, respectively. (D_{km}) is the averaged diffusion coefficient of species k into the mixture m. The details of the evaluation of the thermodynamic and transport properties are gathered in Appendix A.3.

2.2 Tabulated thermodynamic closure

The fully compressible multi-component two-phase flow system described above is closed by a real-fluid EoS and adopting a thermodynamic equilibrium hypothesis, where using a real-fluid EoS is essential at high pressure and temperature conditions far from the ideal gas behavior. In order to consider the phase change phenomenon, the EoS is not sufficient, but a VLE calculation is also included in this study. The main aim of this work is to investigate the evaporation and mixing of fuel droplets in a configuration relevant to dual-fuel, and thus a minimum of three species is required to mimic two different fuels and nitrogen as an air surrogate. Therefore, the current work proposes a pre-tabulation approach, where before the CFD simulation, a 4D-thermodynamic table is generated for a ternary mixture based on the IFPEN-Carnot thermodynamic library. The thermodynamic library performs the VLE calculation using a robust isothermal-isobaric (TP) flash [36] coupled to a real-fluid EoS. Using the IFPEN-Carnot thermodynamic library, it is possible to employ the appropriate EoS (such as PR, CPA) to calculate and tabulate all required properties for the specified ranges of temperature, pressure, and feed of the species. The tabulated properties include the thermodynamic equilibrium density, internal energy, fluid-phase state and composition, and necessary thermodynamic derivatives as heat capacity, sound speed, and transport properties, as described in Appendix A.3.

The thermodynamic table axes are the temperature (T), pressure (P), and species mass fraction ($Y_k, k = 1, ..., N_s - 1$, where N_s is the total number of species). Accordingly, the thermodynamic table is 3D for a binary mixture ($N_s = 2$) and 4D for a ternary mixture ($N_s = 3$) as depicted in the schematic shown in Fig. 2.1.

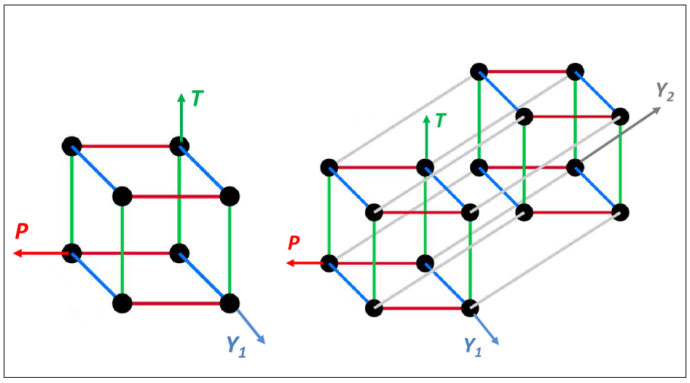

Figure 2.1: 3D table for binary mixture (left) and 4D table for ternary mixture (right), where T: Temperature, P: Pressure , Y_1 : mass fraction of first species, Y_2 : mass fraction of second species.

The interpolation of the 3D and 4D tables is carried out based on the inputs ($T, P, Y_k, k = 1, .., N_s - 1$) using the inverse distance weighting (IDW) method [53]. This method is based on the assumption that the value of the un-sampled point is the average weight of the known values in the neighborhood, and the weight is inversely proportional to the distance between the prediction location and the sampled location. A general form of finding an interpolated value (p) at a given point (x) based on samples $p_i = p(x_i)$ for $i = 1, 2, ..., N$ using IDW can be expressed as follows,

$$p(x) = \begin{cases} \frac{\sum_i^N w_i(x)\, p_i}{\sum_i^N w_i(x)}, & if\ d(x, x_i) \neq 0\ for\ all\ i \\ p_i, & if\ d(x, x_i) = 0\ for\ some\ i \end{cases} \tag{2.5}$$

where $w_i(x) = \frac{1}{d(x,x_i)}$, x denotes an interpolated (arbitrary) point, x_i is an interpolating (known) point, d is the given distance from the known point x_i to the unknown point x, and N is the total number of known points used in interpolation. The thermodynamic table is coupled to the CONVERGE CFD solver [43] as described in the author's recent work [24], where it is used during the simulation for two main tasks:

- Properties look-up: compute the thermal and transport properties, phase state, and composition as a function of $(T, P, Y_k, k = 1, .., N_s - 1)$ obtained from the flow solver.
- Temperature reverse look-up: compute the temperature from the $(e, P, Y_k, k = 1, .., N_s - 1)$ obtained from the flow solver.

The thermodynamic closure of the two-phase system is achieved in this study using a tabulated PR and CPA EoSs to simulate the n-dodecane droplet evaporation in pure nitrogen ambient and mixed (methanol and nitrogen) ambient, respectively. The theoretical formulas of the CPA and PR EoSs along with the different parameters required for each pure compound are detailed in Appendix A.1.

Besides, the accuracy of the VLE computation performed by the thermodynamic library using the CPA and PR EoSs has been validated for two different binary mixtures of the involved species in the current work against published experimental data, as demonstrated in Appendix A.2. The obtained results have shown a satisfactory agreement with the experimental data, which demonstrates the reliability of the thermodynamic library along with the different employed real-fluid EoSs to model the considered mixtures accurately.

3 Description of the simulated test cases

The simulated test cases represent the evaporation of an isolated stationary n-dodecane droplet in quiescent pure nitrogen or mixed (methanol and nitrogen) ambient, where the considered ambient temperatures and pressures are selected to match the typical transcritical conditions that can be found in modern diesel engines and were taken from the experimental work of [11]. The initial conditions of the simulated test cases are summarized in Table. 3.1.

The performed simulations are carried out in two steps. In the first step, the temporal evolution of the n-dodecane droplet evaporation in a pure nitrogen ambient at the reference condition (case 1 in Table. 3.1) is qualitatively compared with the experimental images of [11]. A qualitative comparison is only made since the initial temperature and diameter of the droplet are not known from the experiments. Thereby, the comparison is for the droplet behavior during its lifetime under the same ambient conditions.

In the second step, the n-dodecane droplet evaporation in a mixed (methanol and nitrogen) ambient relevant to the dual-fuel configuration will be investigated at the reference case condition (case 1 in Table 3.1) by adding methanol in the ambient gas with various initial concentrations. Besides, the ambient temperature and pressure are varied to investigate the effect of the methanol ambient concentration on the droplet evaporation at a relatively higher temperature and pressure (case 2 in Table 3.1).

Case	T_{amb} (K)	P_{amb} (bar)	d_o (µm)	$U_{d,o}$ (m/s)	$T_{d,o}$ (K)
1 (Reference case)	700	62	60	0	363
2	1200	106	60	0	363

Table 3.1: Operating conditions of the simulated test cases including the ambient temperature (T_{amb}), ambient pressure (P_{amb}), initial droplet diameter (d_o), initial droplet velocity ($U_{d,o}$), and initial droplet temperature ($T_{d,o}$).

It is worth noting that the current model based on the local thermodynamic equilibrium assumption could lose its validity in the presence of significant non-equilibrium effects, which depend on various factors. Indeed, Miller et al. [37] investigated the significance of thermodynamic non-equilibrium effects on n-decane droplets evaporation as a function of the initial droplet size, gas temperature, and convective droplet Reynolds number. It has been found that non-equilibrium effects are essential for small initial droplet sizes $< 50\,\mu m$. Besides, the influence of non-equilibrium behavior is enhanced under higher gas temperature and convective Reynolds number. Similar investigation to that of [37] has been performed by Yi et al. [58] for ethanol droplets with an initial size range of (20 - 1400 µm), a gas temperature of 723 K and zero Reynolds number. Results showed that the non-equilibrium effects tend to be significant as the initial droplet size is < 50 µm and further increases at 20 µm. According to the previous discussion, non-equilibrium effects could have a contribution to the droplet evaporation under the considered conditions (Table. 3.1), with an initial droplet size of 60 µm, and relatively high gas temperatures. However, the model can still provide valuable insights for the considered droplet size and ambient conditions and their relevant physics. Further investigation of the crucial non-equilibrium effects is essential but requires non-equilibrium two-phase models such as the 7-Equation non-equilibrium model [2, 44, 20].

3.1 Computational set-up and numerical methods

The computational domain comprises a cube of edge length ($10\,d_o$) as depicted in Fig. 3.1a, where the droplet is placed at the domain center and accounts for less than 1% of the domain volume so that the changes in the ambient conditions due to the ongoing evaporation are negligible. The base grid size is set to (16 µm) at the droplet's far-field along with different embedding levels to achieve a mesh resolution at the droplet interior and interface of (2 µm) corresponding to 30 cells/diameter (Fig. 3.1b). The total cell count is approximately 0.55 million cells. The employed grid size is chosen based on a grid sensitivity study using different levels of grid refinement, as will be demonstrated in the next section. Regarding the boundary conditions, the computational domain boundaries (Fig. 3.1a) are set as adiabatic walls with zero gradients for pressure and species mass fraction.

The newly developed RFM model implemented in the CONVERGE CFD code [43] has been used to perform the present simulations. The numerical solution of the transport equations (2.1-2.4) is based on a modified Pressure Implicit with Splitting of Operator (PISO) method [23] for the pressure-velocity coupling. A second-order central difference scheme with flux limiter is used for the spatial discretization of each equation. The time discretization is achieved by the second-order Crank-Nicolson scheme for the momentum equation and the first-order Euler scheme for the rest of the equations. The time step is

automatically controlled by a maximum Courant-Friedrichs-Lewy (CFL) number of 0.9, reaching a value in the range (1 ns−4 ns). The computational cost of the simulation using the newly developed tabulation approach is 48 h of wall clock time for a simulation time of 4 ms using 100 cores of the latest generation Intel Skylake G-6140 processors running at 2.3 GHz (ENER440 IFPEN Supercomputer).

The RFM model thermodynamic closure for the (n-dodecane/ nitrogen) binary mixture is based on the PR-EoS, with thermodynamic table resolution in [P, T, $Y_{C_{12}H_{26}}$] axes of [21×201×101] points, respectively. However, for the droplet evaporation in a mixed ambient, the thermodynamic closure for the (n-dodecane/ nitrogen/ methanol) ternary mixture is based on the CPA-EoS, with thermodynamic table resolution in [P, T, $Y_{C_{12}H_{26}}$, Y_{N_2}] axes is [21×201×101×101] points, respectively. Compared to the PR-EoS, the CPA EoS with its additional association term can be efficiently used to model mixtures including hydrocarbons and polar compounds (methanol) [12].

It is worth noting that the surface tension effect was not considered in the current simulations and assumed to be negligible at the considered high ambient temperatures and pressures. However, this assumption will be further investigated in future work. Indeed, the main objective of this work is to study the effect of the presence of methanol in the ambient medium relevant to the dual-fuel configuration on the evaporation characteristics of an n-dodecane droplet under transcritical conditions.

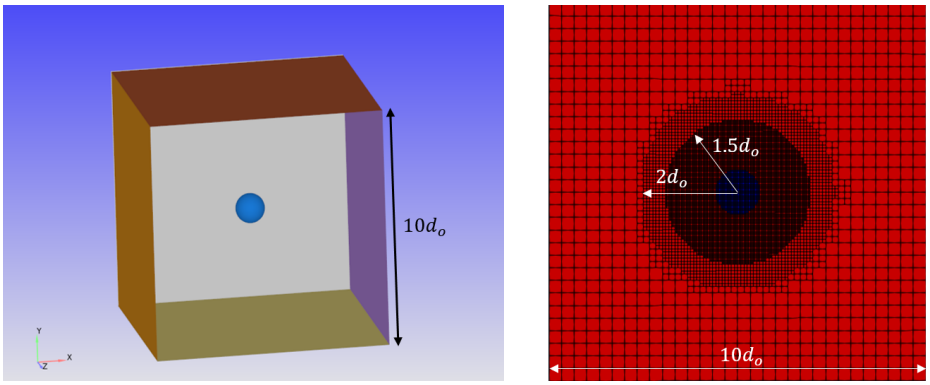

(a) (b)

Figure 3.1: (a) Computational domain size in terms of the initial droplet diameter (d_o), (b) Grid topology with different levels of grid refinement in the central section of the computational domain. The minimum cell size (2 µm) is located at the refinement region with a radius of (1.5 d_o).

3.2 Droplet evaporation in pure nitrogen at the reference condition

A grid sensitivity study is performed at the reference case condition using different grid refinement levels to achieve a minimum cell size of (4, 2, 1 µm) corresponding to (15,

30, 60 cells/diameter) at the droplet interior and interface. Fig. 3.2 shows that a grid independent solution is achieved for the dimensionless droplet volume (V/V_o) temporal evolution with the grid of minimum cell size of (30 cells/diameter). Accordingly, it has been employed for further calculations as a compromise between accuracy and computational cost.

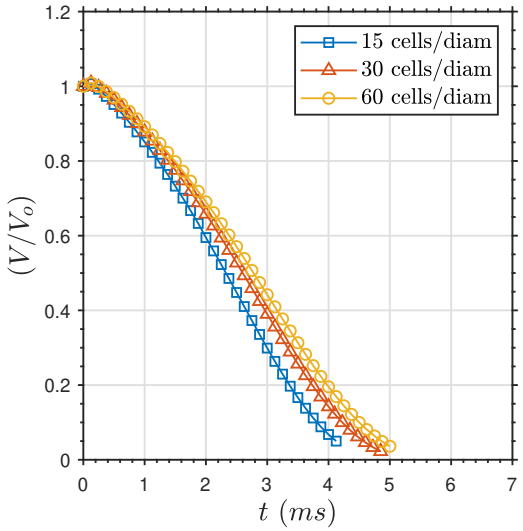

Figure 3.2: Temporal evolution of the dimensionless droplet volume (V/V_o) for case 1 ($P_{amb} = 62\,\text{bar}$, $T_{amb} = 700\,\text{K}$) using different levels of grid refinement.

The temporal evolution of the n-dodecane droplet evaporation under the reference condition (Table 3.1) is qualitatively compared with the experimental images [11] under the same ambient conditions.

Fig. 3.3 shows the temporal variation of the liquid volume fraction (α_L) obtained from the simulation at the central cut-section of the droplet compared with the experimental images. The initial time of the comparison is similar to that of the published experimental video sequence ($\text{t} \approx 0.03\,\text{ms}$). Overall a good qualitative agreement can be observed. Indeed, the droplet is decreasing in size due to the ongoing evaporation, as illustrated by the blue isoline of ($\alpha_L = 0.5$) depicted on the simulation images. This comparison shows that the RFM model proposed in this work is capable of providing detailed characteristics of droplet evaporation under such transcritical conditions and can therefore be applied with sufficient confidence to the study of ternary mixtures that are more representative of the dual-fuel configuration.

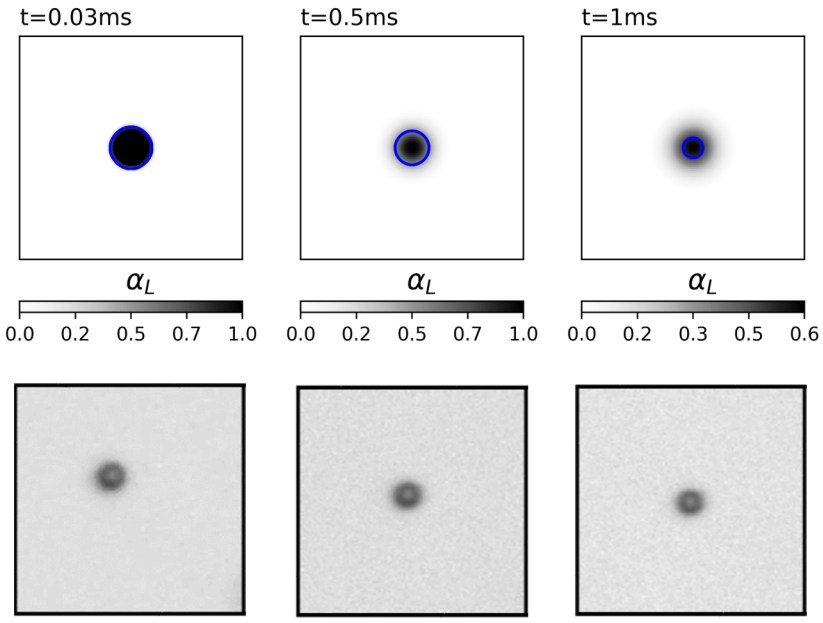

Figure 3.3: Qualitative comparison of the temporal evolution of the liquid volume fraction (α_L) obtained from the simulation in the central cut-section of the evaporating n-dodecane droplet (first row) with the experimental images [11] (second row) under the same ambient conditions ($P_{amb} = 62\,\text{bar}$, $T_{amb} = 700\,\text{K}$). The blue line depicted on the simulation images represents an isoline of ($\alpha_L = 0.5$). The size of the numerical images is ($300\,\mu\text{m} \times 300\,\mu\text{m}$) similar to the experimental ones. The initial time of the comparison is similar to that of the published experimental video sequence ($\text{t} \approx 0.03\,\text{ms}$).

4 Droplet evaporation in dual-fuel configuration

4.1 Effect of the methanol ambient concentration

In this section, the n-dodecane droplet is evaporating in a homogeneously mixed ambient of Nitrogen (N_2) and methanol (CH_3OH) at the same ambient pressure and temperature as the reference case (case 1 in Table 3.1). However, the initial methanol mass fraction (Y_{CH_3OH}) in the ambient mixture is varied from 0.2 to 0.6, and accordingly, the initial mass fraction of nitrogen in the ambient is ($Y_{N_2} = 1 - Y_{CH_3OH}$).

The effect of the methanol ambient concentration on the temporal variation of the dimensionless squared droplet diameter $(d/d_o)^2$ is depicted in Fig. 4.1a. In this figure, the droplet diameter is computed from the simulations based on the liquid volume (V_L) as $[d = (6/\pi \sum_{cells} \alpha_L V_{cell})^{1/3}]$. Two main observations can be drawn from this figure. On the one hand, a higher methanol ambient concentration causes a greater rise in the droplet size during the early evaporation phase. On the other hand, a reduction in droplet lifetime can be observed with increasing methanol ambient concentration compared to the reference case ($Y_{CH_3OH} = 0$).

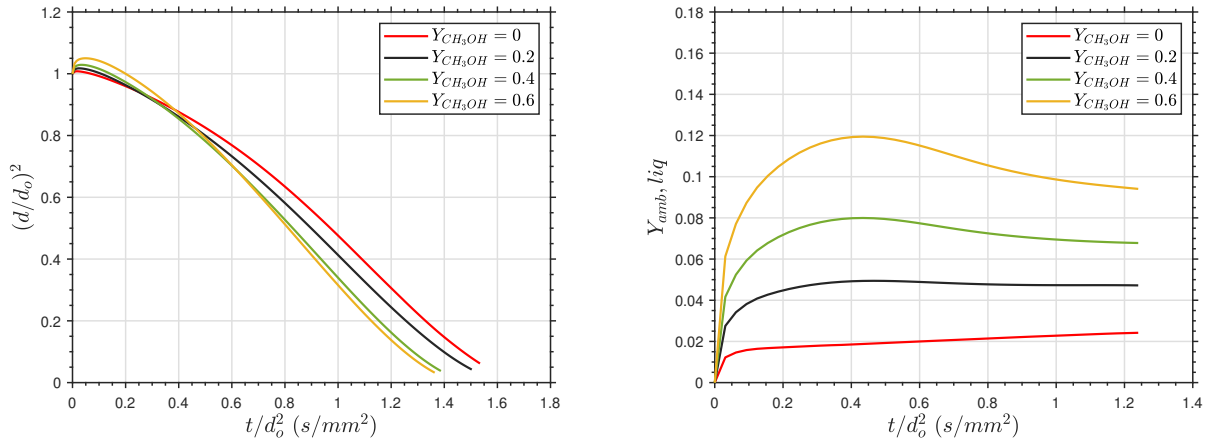

(a) (b)

Figure 4.1: (a) Temporal evolution of the dimensionless squared droplet diameter $(d/d_o)^2$, and (b) mean mass fraction of dissolved ambient gases (methanol + nitrogen) in the liquid phase ($Y_{amb,liq}$) at ($P_{amb} = 62\,\text{bar}$, $T_{amb} = 700\,\text{K}$) for different methanol ambient concentrations (Y_{CH_3OH}).

Regarding the initial droplet size increase, this phenomenon has been classically attributed to the liquid thermal expansion at the beginning of the evaporation [**?**]. However, in the current study, a larger droplet size increase at the beginning of the evaporation is found by increasing the methanol ambient concentration. This behavior can be explained through Fig. 4.1b, which shows the temporal evolution of the mean mass fraction of dissolved ambient gases (methanol + nitrogen) in the liquid phase ($Y_{amb,liq}$), computed as $\left[Y_{amb,liq} = \frac{\sum_{cells}(Y_{CH_3OH,liq}+Y_{N_2,liq})\alpha_l V_{cell}}{\sum_{cells}\alpha_l V_{cell}}\right]$, where ($Y_{CH_3OH,liq}$) and ($Y_{N_2,liq}$) are the mass fraction of methanol and nitrogen dissolved in the liquid phase, respectively. An increase of the mean mass fraction of dissolved ambient gases can be observed throughout the droplet lifetime with increasing the methanol ambient concentration, which would explain the initial droplet size increase behavior (Fig. 4.1a). Besides, this behavior demonstrates that methanol exhibits a relatively higher solubility in the liquid phase compared to nitrogen. Fig. 4.1b also shows a non-trivial amount of dissolved gases, which emphasizes that considering the solubility of the ambient gases in the liquid phase at such high-pressure conditions is essential and cannot be neglected, for instance, in Lagrangian droplets evaporation models.

Fig. 4.2a presents the temporal variation of the mean droplet temperature (T_d) computed from the simulations as $\left[T_d = \frac{\sum_{cells} T_{cell}\alpha_l V_{cell}}{\sum_{cells}\alpha_l V_{cell}}\right]$, where ($T_{cell}$) is the cell temperature. It can be seen that the mean droplet temperature is relatively higher throughout the droplet lifetime for higher methanol ambient concentrations. This temperature trend suggests that the droplet follows a different thermodynamic path based on the methanol ambient concentration.

For further understanding of the mean droplet temperature behavior, Fig. 4.2b shows

the adiabatic mixing temperature (T_{AM}) variation with the fuel (n-dodecane) mole fraction along with the two-phase region for the different methanol ambient concentrations. The adiabatic mixing temperature is formulated as,

$$h_{mix}(T_{AM}, P_{amb}, Y_{C_{12}H_{26}}) = Y_{C_{12}H_{26}}\, h_{C_{12}H_{26}}(T_{C_{12}H_{26}}, P_{amb}) + Y_{amb}\, h_{N_2}(T_{amb}, P_{amb}) \quad (4.1)$$

where h, $Y_{C_{12}H_{26}}$, Y_{amb} are the specific enthalpy, mass fraction of the n-dodecane, and the ambient gases, respectively. $T_{C_{12}H_{26}}$, T_{amb}, P_{amb} denote the initial temperature of the fuel (n-dodecane), the initial temperature of the ambient, and the ambient pressure, respectively. The ambient mass fraction is formulated as ($Y_{amb} = Y_{CH_3OH} + Y_{N_2}$), where $Y_{CH_3OH} = C\ Y_{amb}$, $Y_{N_2} = (1 - C)\ Y_{amb}$, and $C = \{0, 0.2, 0.4, 0.6\}$. The adiabatic mixing temperature is computed taking into account the phase change based on the VLE solver. Fig. 4.2b shows the variation of the adiabatic mixing temperature as a function of the fuel (n-dodecane) mole fraction. The (T_{AM}) starts at the initial droplet temperature (363 K) on the right-hand side and increases to the ambient temperature (700 K) on the left-hand side. It can be seen that the adiabatic mixing temperature is relatively higher with increasing the methanol ambient concentration, which would explain the mean droplet temperature trend obtained from the simulations (see Fig. 4.2a). Besides, Fig. 4.2b shows that the two-phase region along the adiabatic mixing temperature lines shrinks noticeably as methanol ambient concentration increases, which would contribute to the relative reduction of the droplet lifetime observed in Fig. 4.1a.

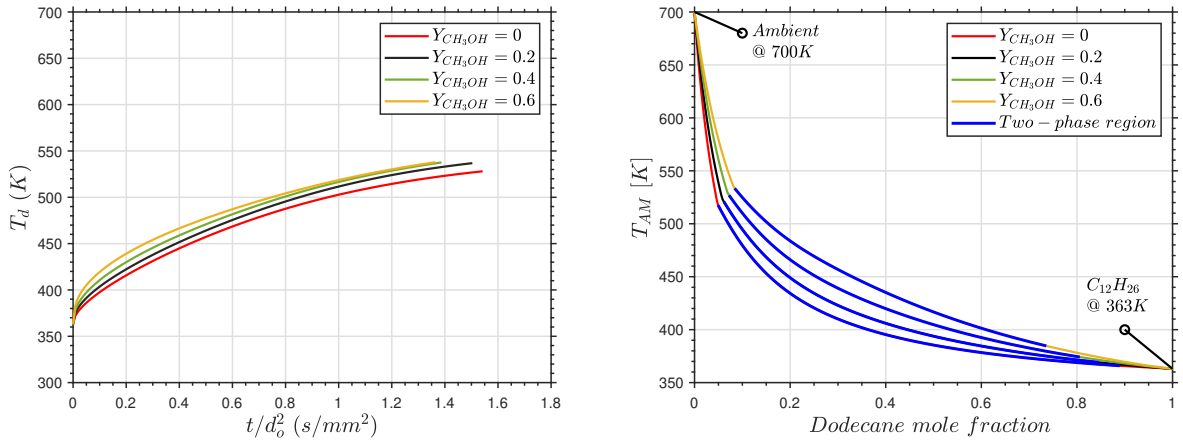

(a) (b)

Figure 4.2: (a) Temporal evolution of the mean droplet temperature (T_d) and (b) adiabatic mixing temperature (T_{AM}) along with the two-phase region represented by the blue lines at ($P_{amb} = 62\,\text{bar}$, $T_{amb} = 700\,\text{K}$) for different methanol ambient concentrations (Y_{CH_3OH}). The blue lines in (b) show how the two-phase region shrinks as the methanol increases in the ambient gas. The right side of (b) shows a smaller dodecane mole fraction at the start of the two-phase region (ie. higher mole fraction of dissolved gases in the liquid phase) as the methanol ambient concentration increases.

4.2 Effect of the ambient temperature and pressure

The effect of the variation of the ambient temperature and pressure on single or multi-component droplet evaporation has been extensively investigated in the literature [19, 14, 3, 25], whereas, in the current study, the main focus is to monitor the methanol ambient concentration effect on the droplet evaporation characteristics at various ambient temperatures and pressures. Accordingly, the impact of the methanol ambient concentration is investigated at a higher ambient temperature and pressure (case 2 in Table 3.1) compared to the reference case condition (case 1 in Table 3.1).

Fig. 4.3a shows the temporal variation of the dimensionless squared droplet diameter for the second ambient condition. It can be seen that the droplet exhibits a relatively higher evaporation rate and shorter lifetime as the methanol ambient concentration increases. Besides, Fig. 4.3b shows a higher total amount of dissolved ambient gases than the reference case (Fig. 4.1b) as the ambient pressure and temperature increase.

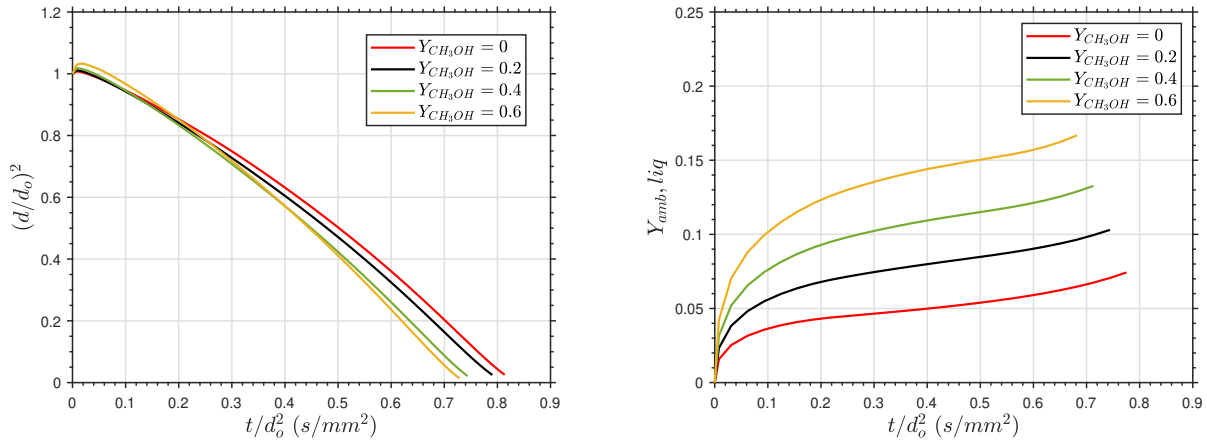

(a) (b)

Figure 4.3: (a) Temporal evolution of the dimensionless squared droplet diameter $(d/d_o)^2$ and (b) mean mass fraction of dissolved ambient gases (methanol + nitrogen) in the liquid phase ($Y_{amb,liq}$) at ($P_{amb} = 106\,\text{bar}$, $T_{amb} = 1200\,\text{K}$) for different methanol ambient concentrations (Y_{CH_3OH}).

The temporal variation of the mean droplet temperature (Fig. 4.4a) for the different methanol ambient concentrations tends to follow the adiabatic mixing temperature variation depicted in Fig. 4.4b. In addition, the relative reduction of the two-phase region along the adiabatic mixing temperature curves (Fig. 4.4b) with increasing the methanol ambient concentration is more significant than the reference case (Fig. 4.2b) at lower ambient pressure and temperature.

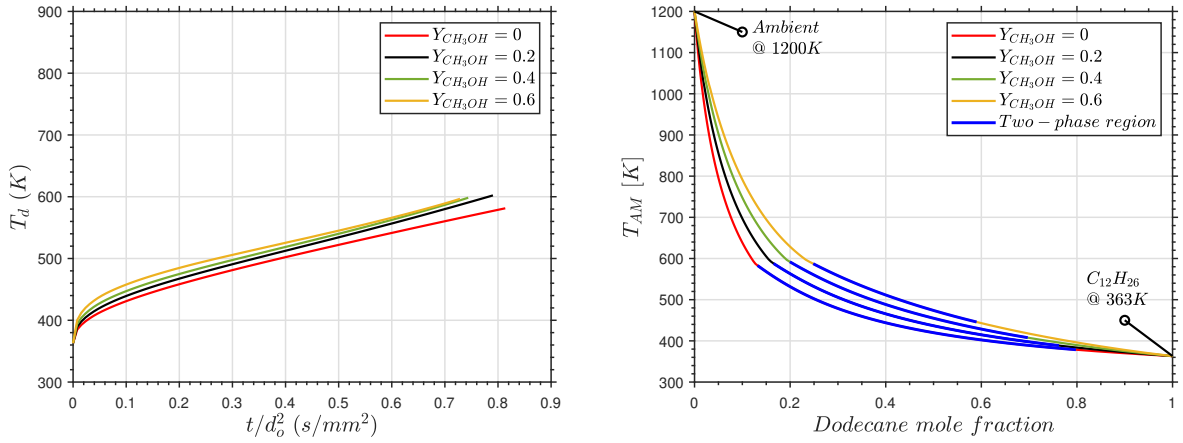

(a) (b)

Figure 4.4: (a) Temporal evolution of the mean droplet temperature (T_d) and (b) adiabatic mixing temperature (T_{AM}) along with the two-phase region represented by the blue lines at ($P_{amb} = 106\,\text{bar}$, $T_{amb} = 1200\,\text{K}$) for different methanol ambient concentrations (Y_{CH_3OH}).

Fig. 4.4a also shows that the mean droplet temperature keeps increasing during the entire droplet lifetime without reaching a steady temperature, the so-called wet-bulb tem-

perature for the different methanol ambient concentrations. This behavior has also been observed in the literature [25, 27] when the ambient pressure is higher than the fuel critical pressure. It can be attributed to the simultaneous occurrence of the droplet vaporization and heating-up processes, due to the relatively low latent heat of vaporization, in contrast to the low or moderate pressure conditions, where the droplet heating process takes place almost separately from the vaporization process. The behavior of not reaching a steady temperature can also be seen through Fig. 4.2a at the reference case condition, but it is more pronounced at the ambient conditions of case 2 (Fig. 4.4a).

To summarize the results of the considered ambient conditions, the droplet evaporation characteristics are evaluated in terms of evaporation rate constant (k), initial heat-up time (t_H), and droplet lifetime (t_L). The definitions of $(k, t_H/d_o^2, t_L/d_o^2)$ are similar to previous experimental [17, 38] and numerical [19, 56] studies as illustrated in Fig. 4.5. The evaporation rate constant is defined as the slope of the best-fit straight line obtained by the least-squares linear fitting method in the range of $(d/d_o^2) = (0.1 - 0.8)$, after the initial heat-up period. The time at the intersection point of the fitting line and the straight line $(d/d_o^2 = 1)$ is regarded as the initial heat-up time, whereas the time at the intersection point of the fitting line and the straight line $(d/d_o^2 = 0)$ is regarded as the droplet lifetime. The previous definition of (k) is adopted (instead of mass evaporation rate $(\dot{m})$) in the current analysis, as it can be directly determined from the droplet diameter temporal evolution obtained from the simulation (see Fig. 4.5). In addition, a mass evaporation rate can be deduced from (k) using $(\dot{m} = -\rho_m \frac{\pi}{4} k D)$ as demonstrated in [18], where (ρ_m) is assumed to be a constant mean density of the liquid droplet. Thus, to avoid such assumption, only (k) was considered for the analysis of the current results.

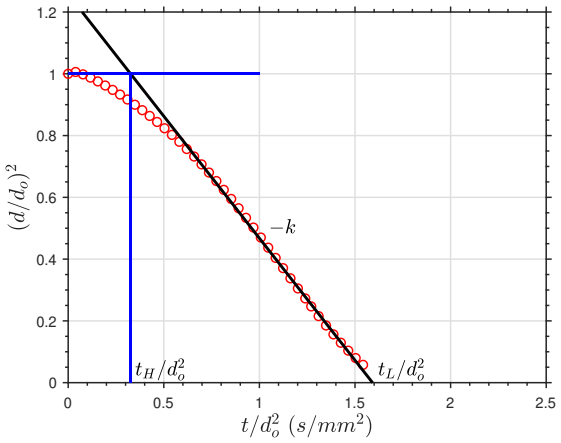

Figure 4.5: Definition of the droplet evaporation rate (k), initial heat-up time (t_H) and lifetime (t_L) at $(P_{amb} = 62\,\text{bar}, T_{amb} = 700\,\text{K}, Y_{CH_3OH} = 0)$.

Fig. 4.6 shows the variation of $(k, t_H/d_o^2, t_L/d_o^2)$ as a function of the initial methanol ambient concentration (Y_{CH_3OH}) for the considered ambient conditions. Fig. 4.6c shows that the droplet lifetime decreases monotonically with increasing methanol ambient con-

centration. The droplet evaporation rate and heat-up time variation with the methanol ambient concentration are investigated to further understand the droplet lifetime behavior. The contribution of the evaporation rate and initial heat-up time to the droplet lifetime can be understood through Eq. 4.2, where the droplet lifetime is written as the sum of the heat-up time and the inverse of the evaporation rate constant.

$$t_L/d_o^2 = t_H/d_o^2 + 1/k \tag{4.2}$$

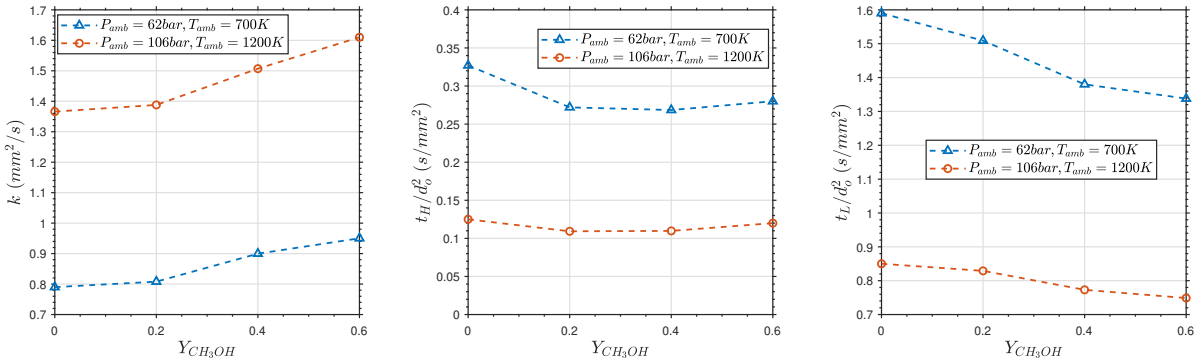

(a) (b) (c)

Figure 4.6: Variation of the (a) evaporation rate constant, (b) initial heat-up time, and (c) evaporation lifetime with the initial methanol ambient concentration (Y_{CH_3OH}) at different ambient temperatures (T_{amb}) and pressures (P_{amb}). The droplet evaporation lifetime and the initial heat-up time are divided by the squared initial droplet diameter d_o^2.

Fig. 4.6a shows a monotonic increase of the evaporation rate with increasing the methanol ambient concentration. This behavior can be explained through Fig. 4.7, which shows the equilibrium mole fraction of vaporous n-dodecane (fuel) at the two-phase states along the adiabatic mixing temperature curves (bold blue lines of Figs. (4.2b, 4.4b)). A relative increase in mole fraction of vaporous n-dodecane can be observed as the methanol ambient concentration increases, which is accompanied by a higher spatial gradient of the vaporous n-dodecane outside the droplet, enhancing the mass transport away from the droplet. Besides, the increase of the ambient mixture thermal conductivity (Fig. 4.8a) as the methanol ambient concentration increases, would contribute to the increase of the evaporation rate (Fig. 4.6a).

Regarding the initial heat-up time depicted in Fig. 4.6b, it shows an initial decrease with increasing the methanol ambient concentration, then it tends to be less sensitive to the variation of the methanol ambient concentration and eventually tends to slightly increase at ($Y_{CH_3OH} = 0.6$). The increase of the ambient mixture thermal conductivity with the methanol ambient concentration would contribute to the reduction of the heat-up time. Meanwhile, Figs. (4.2b, 4.4b) shows that, as the methanol ambient concentration increases, the droplet will be heated to a higher temperature before entering the two-

phase region, which would contribute to a longer heat-up time. Accordingly, the above competing mechanisms would determine the heat-up time.
Thus, for the considered transcritical conditions, the contribution of the evaporation rate and the heat-up time leads to a monotonic reduction of the droplet lifetime with increasing the methanol ambient concentration.

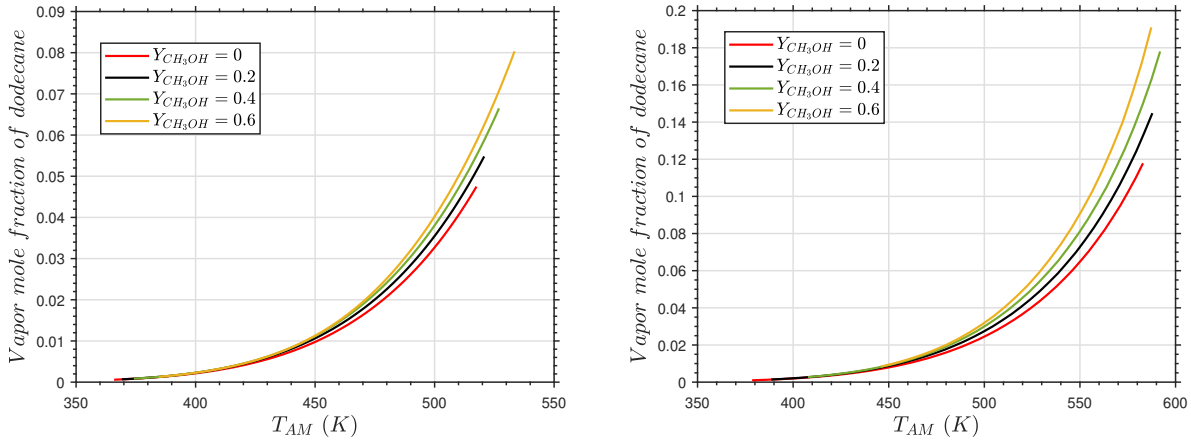

Figure 4.7: Variation of the equilibrium mole fraction of vaporous n-dodecane in the two-phase region along the adiabatic mixing temperature lines for the various methanol ambient concentrations (Y_{CH_3OH}) at (a) ($P_{amb} = 62\,\text{bar}$, $T_{amb} = 700\,\text{K}$), (b) ($P_{amb} = 106\,\text{bar}$, $T_{amb} = 1200\,\text{K}$).

For a given methanol ambient concentration, the droplet lifetime decreases, with increasing the (P_{amb}, T_{amb}) as shown in Fig. 4.6c. This reduction in the droplet lifetime is consistent with the increase in the evaporation rate (Fig. 4.6a) and the reduction of the heat-up time (Fig. 4.6b) as the ambient pressure and temperature increase compared to the reference case condition ($P_{amb} = 62\,\text{bar}$, $T_{amb} = 700\,\text{K}$).

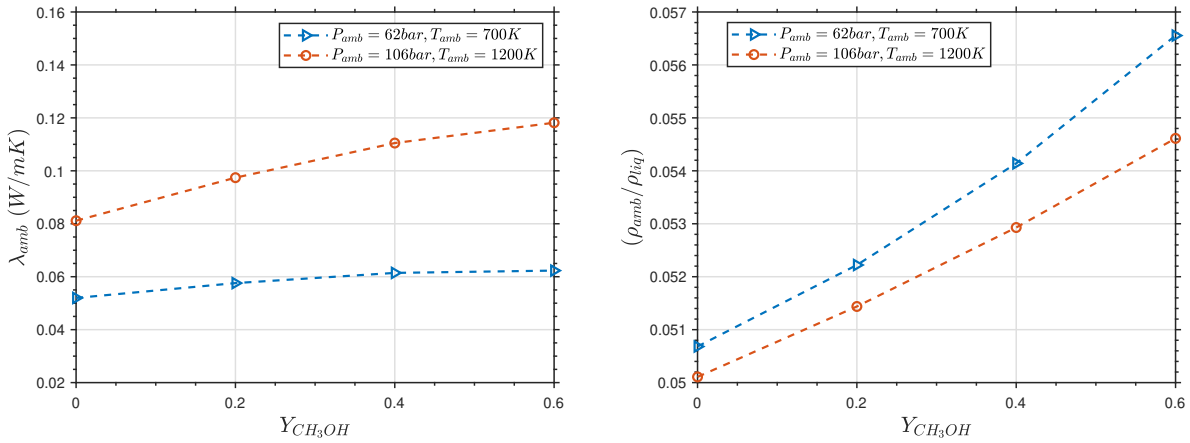

(a) (b)

Figure 4.8: Variation of (a) the ambient mixture thermal conductivity (λ_{amb}) and (b) the ambient gas to liquid phase density ratio (ρ_{amb}/ρ_{liq}) as a function of the methanol ambient concentration (Y_{CH_3OH}) at the ambient temperatures (T_{amb}) and pressures (P_{amb}) considered and the initial droplet temperature (363 K).

It is worth mentioning that the increase of the methanol ambient concentration is accompanied by an increase in the gas-phase density for a given ambient temperature and pressure. Thus, the gas to liquid phase density ratio increases as the methanol ambient concentration increases, as shown in Fig. 4.8b. The densities of the gas and liquid phases are computed for a given ambient pressure and initial temperature of the ambient gas and liquid droplet, respectively. This increase of the gas to liquid phase density ratio implies that the widely used gas-phase quasi-steady assumption in classical droplet evaporation models needs to be revised in such transcritical conditions as the density ratio increases towards unity [25].

In addition, the thermodynamic analysis has shown that droplet exhibits two-phase states during its lifetime (see Figs. (4.2b, 4.4b)), and the evaporation doesn't take place entirely in a supercritical regime, although the considered ambient temperatures and pressures are higher than the critical point of pure n-dodecane (T_c = 658.1 K, P_c = 18.2 bar). This behavior is due to the multi-component mixture critical point variation compared to that of the pure component. For instance, Yi et al. [59] have demonstrated that the transition from subcritical evaporation to diffusive mixing regime, is based on the mixture's critical point for the multi-species problem, not the pure-fuel critical point. It also implies that considering the vapor-liquid equilibrium theory is essential for the correctness of the modeling as subcritical and supercritical states may exist simultaneously based on the local temperature, pressure, and species composition [24, 57, 35].

5 Conclusions

This work presents a real fluid modeling approach applied to ternary mixtures relevant to dual-fuel internal combustion engine configuration. The Real-fluid model (RFM) employed by the IFPEN group [24] is based on a two-phase fully compressible four-equation model under mechanical, thermal, and thermodynamic equilibrium assumptions. In the current study, the RFM model tabulation approach is further developed to ternary mixtures tabulation, where the IFPEN-Carnot thermodynamic library is used to generate the thermodynamic tables. The thermodynamic library employs a robust isothermal-isobaric (TP) flash coupled with different real-fluid EoS to compute the required thermodynamic and transport properties as well as the phase state and composition. The RFM model tabulation approach has been implemented in the CONVERGE CFD code. The main goal of the current work is to investigate the evaporation characteristics of a single n-dodecane droplet in a bi-component ambient (methanol + nitrogen) through highly resolved simulations considering the real-fluid thermodynamics. The RFM model closed by a tabulated CPA EoS has been employed to investigate the effect of the methanol ambient concentration on the droplet evaporation at various transcritical ambient conditions. The main conclusions obtained in this study include:

- A qualitative comparison of the numerical results with the experiments [11] has shown that the RFM model can capture well the evolution of the n-dodecane droplet evaporation throughout its lifetime under the considered transcritical conditions.

- For the considered ambient temperatures and pressures, the n-dodecane droplet lifetime decreases monotonically with increasing the methanol ambient concentration. The thermodynamic analysis shows that the droplet follows a different thermodynamic path based on the methanol ambient concentration. The different mechanisms contributing to the droplet lifetime behavior have been thoroughly discussed.

- A higher droplet size increase at the initial stage of the evaporation process has been found with increasing the methanol concentration for a given ambient temperature and pressure, which can be attributed to a relatively higher solubility of methanol in the liquid phase compared to that of nitrogen.

- Increasing the ambient temperature and pressure is accompanied by a more significant reduction of the two-phase region along the adiabatic mixing temperature lines and an increase of the dissolved ambient gases.

- The methanol and nitrogen exhibit different behavior in terms of solubility in the liquid phase, which demonstrates that these two compounds cannot be lumped in a single surrogate.

- The droplet exhibited two-phase states during its lifetime even if the considered ambient temperatures and pressures are higher than the n-dodecane critical point, which implies that considering the vapor-liquid equilibrium theory is indeed required for the correct modeling of such transcritical conditions.
- For a given ambient temperature and pressure, the gas to liquid phase density ratio increases as the methanol ambient concentration increases, suggesting that the widely used quasi-steady gas-phase assumption in classical evaporation models could be revised for such conditions, where the density ratio is not small compared to unity.
- The newly developed RFM model closed by a tabulated CPA EoS for ternary mixtures shows great potential for the computation of two-phase multi-component mixtures problems, avoiding the direct evaluation of costly phase equilibrium solver during the simulation run-time [57].
- The obtained results could be used to further adjust or develop improved Lagrangian droplet evaporation models for such dual-fuel configurations.

Acknowledgments

This project has received funding from the European Union Horizon 2020 Research and Innovation programme. Grant Agreement No 861002. The authors would like to acknowledge Dr. Angela Di-lella for the development of the thermodynamic table generator tool based on IFPEN-Carnot library and the continuous support to resolve the encountered technical issues.

A Appendix

A.1 Real-fluid equations of state (EoS)

The theoretical formulas of the Cubic Plus Association (CPA) [31] and Peng-Robinson (PR) [41] equations of state are detailed in the current section to highlight the differences between these two EoSs. Compared to the PR-EoS, the CPA-EoS combines the cubic Soave–Redlich–Kwong (SRK) EoS [50] and an association term for modeling of associating compounds. Thus, in the absence of associating compounds, the SRK cubic equation is recovered, and the existing cubic EoS correlations can be used

Generally, the EoS formulation (Equation (A.1)) includes repulsive and attractive contributions, and it may have additional contributions, such as the association contribution included in the CPA EoS. The different contributions are introduced in Table (A.1) for the two EOSs.

$$P = repulsive\,contribution + attractive\,contribution + association\,contribution \quad \text{(A.1)}$$

EOS	repulsive contribution	attractive contribution	association contribution
PR	$\frac{RT}{v-b}$	$-\frac{a(T)}{v\,(v+b)+b\,(v-b)}$	–
CPA	$\frac{RT}{v-b}$	$-\frac{a(T)}{v\,(v+b)}$	$-\frac{1}{2}\frac{RT}{v}\left(1+\rho\frac{\partial \ln g}{\partial \rho}\right)\sum_i x_i \sum_{A_i}(1-X_{A_i})$

Table A.1: Expressions for the different contributions in the EOS

where R is the ideal gas constant, T is the temperature, v is the molar volume, $a(T)$ is the energy parameter, b is the co-volume parameter, ρ is the molar density, g is the radial distribution function, X_{A_i} is the mole fraction of molecule i not bonded at site A and x_i is the mole fraction of the component i. The key element of the association term is X_{A_i} which is related to the association strength $\Delta^{A_iB_j}$ between 2 sites belonging to two different molecules (e.g. site A on molecule i and site B on molecule j) is expressed as:

$$X_{A_i} = \frac{1}{1+\rho\sum_i x_j \sum_{B_j} X_{B_j}\Delta^{A_iB_j}}$$

where the association strength term in the CPA EoS is expressed as:

$$\Delta^{A_iB_j} = g(\rho)\left[\exp\left(\frac{\varepsilon^{A_iB_j}}{RT}\right)-1\right]b_{ij}\beta^{A_iB_j}$$

with the radial distribution function ($g(\rho)$) and b_{ij} expressed as:

$$g(\rho) = \frac{1}{1-1.9\eta},\ \eta = \frac{1}{4}b\rho,\ b_{ij} = \frac{b_i+b_j}{2}$$

The energy parameter $a_i(T)$ of the EoS for a pure component (i) is formulated as:

$$a_i(T) = (a_0)_i\left[1+(c_1)_i\left(1-\sqrt{T_\mathrm{r}}\right)\right]^2, T_r = \frac{T}{T_c}$$

where T_c is the critical temperature.

The parameters $\varepsilon^{A_iB_j}$and $\beta^{A_iB_j}$ are called the association energy and the association volume, respectively. These two parameters are only used for associating components such as alcohols and, together with the three parameters of the SRK term (a_o, b, c_1), represent the five pure compound parameters of the CPA model. They are usually obtained by fitting vapor pressure and liquid density data. However, for inert components such as hydrocarbons, only the three parameters (a_o, b, c_1) of the SRK term are required, which can be obtained either from vapor pressures and liquid densities or calculated based on

the critical point (T_c, P_c) and the acentric factor (ω) similar to the PR EoS as presented in Table (A.2).

EOS	$(a_o)_i$	b_i	$(c_1)_i$
PR	$0.45724\frac{R^2T_c^2}{P_c}$	$0.07780\frac{RT_c}{P_c}$	$0.37464 + 1.5422\omega - 0.26992\omega^2$
CPA	$0.42747\frac{R^2T_c^2}{P_c}$	$0.08664\frac{RT_c}{P_c}$	$0.48508 + 1.55171\omega - 0.15613\omega^2$

Table A.2: Pure component parameters used in the CPA (for non-associating compounds) and PR EOSs

when the CPA or the PR EoS are used for mixtures, Van-der Waals mixing rules are applied for the energy and co-volume parameters $(a(T), b)$ as:

$$a(T) = \sum_i \sum_j x_i\, x_j a_{ij}(T)$$

$$a_{ij}(T) = \sqrt{a_i(T) a_j(T)}\,(1 - k_{ij}) \tag{A.2}$$

$$b = \sum_i x_i\, b_i$$

where (k_{ij}) is the binary interaction parameter that can be fitted to experimental data to well represent the phase diagram of a binary system.

A.2 Validation of the vapor-liquid equilibrium (VLE) computation

The current section presents a validation of the vapor-liquid equilibrium (VLE) calculation using the IFPEN-Carnot thermodynamic library in conjunction with the employed real-fluid EOSs. The VLE is computed for two different binary mixtures of the species involved in the current simulations and compared with available experimental data. The VLE of a binary mixture of (n-dodecane/nitrogen) is computed for using the PR EoS with a binary interaction parameter ($k_{ij} = 0.19$) and compared with the experimental data [15]. The critical parameters for each pure compound are summarized in Table. A.3. The comparison of the calculation results with the experimental data for the different iso-therms is depicted in Fig. A.1a, showing a satisfactory agreement between the calculations and the experiments for the majority of the considered pressures.

Besides, the VLE of a binary mixture of (methanol/nitrogen) has been computed using the CPA EoS and compared against the experimental data [6]. The CPA EoS parameters for methanol are listed in Table. A.4. Fig. A.1b presents the comparison of the calculation results with the experimental data. It shows that the VLE calculation agrees well with the experimental data for the different iso-therms, which demonstrates the reliability of the CPA EoS with its additional association term to model mixtures including polar

compounds (methanol).

The performed VLE calculations illustrate the reliability of the IFPEN-Carnot thermodynamic library along with the different real-fluid EoSs to accurately model the considered mixtures.

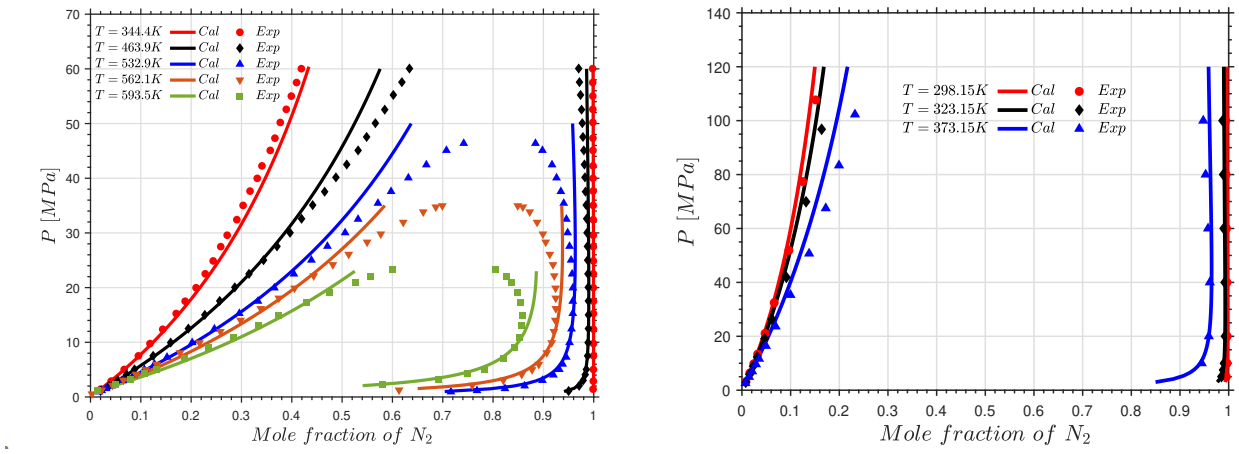

(a) (b)

Figure A.1: Phase diagram of binary mixtures (a) n-dodecane ($C_{12}H_{26}$) and nitrogen (N_2) using PR EoS, (b) methanol (CH_3OH) and nitrogen (N_2) using CPA EoS.

Species	T_c (K)	P_c (bar)	ω
n-dodecane	658.1	18.2	0.57344
nitrogen	126.2	33.9	0.0403

Table A.3: Critical parameters of n-dodecane and nitrogen including, the critical temperature (T_c), critical pressure (P_c), and the acentric factor (ω).

a_o (Pa.m^3/mol)	c_1	b (m^3/mol)	ϵ^{OH}/R (Pa.m^3/mol)	β^{OH}
0.40531	0.431	3.1e-05	2957.604	0.0161

Table A.4: CPA EoS parameters for the polar compound (methanol).

A.3 Thermodynamic and transport properties

The calculation of the thermodynamic properties is performed based on the residual approach [12]. In this approach, any thermodynamic function (f) is computed from the sum of an ideal gas part (f^o) and a residual part (f^{res}). The ideal gas part is determined from a specific polynomial equation [39] . While the residual part, which represents the deviation from the ideal gas behavior is deduced from the employed equation of state (EoS).

Regarding the evaluation of the transport properties, the thermal conductivity (λ) and dynamic viscosity (μ) are computed by the Chung et al. [10] correlations. The binary diffusion coefficients (D_{kj}) are calculated in CONVERGE [43] as $[ln\, D_{kj} = \sum_{n=1}^{N} d_{n,kj}(ln\, T)^{n-1}]$, where ($T$) is the temperature and ($d_{n,kj}$) are the diffusion parameters. Then, the mixture averaged diffusion coefficient of species k into the mixture (D_{km}) is obtained from the binary diffusion coefficients according to [30] as $[\frac{1}{D_{km}} = \sum_{j\neq k}^{K} \frac{X_j}{\mathcal{D}_{kj}} + \frac{X_k}{1-Y_k} \sum_{j\neq k}^{K} \frac{Y_j}{\mathcal{D}_{kj}}]$, where X and Y are the mole fraction and mass fraction of the species, respectively. The (D_{km}) is obtained at pressures other than unity by dividing the calculated diffusion coefficient by the actual pressure.

The tabulated two-phase mixture properties are computed from the liquid and gas phase properties as described through Equations (A.3-A.9)

$$\rho = \sum_{p} \alpha_p \rho_p \tag{A.3}$$

$$e = \frac{1}{\rho} \sum_{p} \alpha_p \rho_p e_p \tag{A.4}$$

$$\lambda = \frac{1}{\rho} \sum_{p} \alpha_p \rho_p \lambda_p \tag{A.5}$$

$$\mu = \sum_{p} \alpha_p \mu_p \tag{A.6}$$

$$C_p = \frac{1}{\rho} \sum_{p} \alpha_p \rho_p C_{p_p} \tag{A.7}$$

$$C_v = \frac{1}{\rho} \sum_{p} \alpha_p \rho_p C_{v_p} \tag{A.8}$$

$$\frac{1}{\rho C^2_{s,mix,Wood}} = \sum_{p} \frac{\alpha_p}{\rho_p C^2_{s,p}} \tag{A.9}$$

where (α_p) is the phase volume fraction and ($p = l, v$) stands for liquid and vapor phases, respectively. ($\rho, e, \lambda, \mu, C_p, C_v, C_{s,mix,Wood}$) are the two-phase mixture density, specific internal energy, thermal conductivity, dynamic viscosity, specific heats at constant pressure and volume, and Wood speed of sound [55], respectively. Fig. A.2 shows the variation of the mixture thermodynamic and transport properties for the ternary mixture of (n-dodecane/nitrogen/methanol) at $P = 106\,\text{bar}$ and $T = 500\,\text{K}$. These results show the variation of the different properties as a function of the species composition. Besides, it demonstrates that the employed real-fluid EoS can capture the non-linearity of some properties at the considered transcritical regime. Indeed, Fig. A.2e shows the peak of the isobaric heat capacity, which takes place around the widom-line [4] in the region,

where the methanol mole fraction is approaching unity. In addition, Fig. A.3 depicts the pressure-temperature diagram of pure methanol colored with the density and the isobaric heat capacity. It shows that the point ($P = 106\,\mathrm{bar}$ and $T = 500\,\mathrm{K}$) is located at the vicinity of the widom line, where the isobaric heat capacity starts to increase and reaches a peak value when crossing the widom line. It is important to note that calculating the mixture's specific heats (C_p, C_v) in the VLE region is done by linearly blending the liquid and vapor phases specific heats [42, 59]. However, it has been recently demonstrated by Tudisco and Menon [52] that such an approach leads to significant departures from the actual definition of the specific heats. Besides, they showed that the sound speed computed from the Wood formula could exhibit low accuracy. Thereby, in future work, a more accurate evaluation of such properties will be considered.

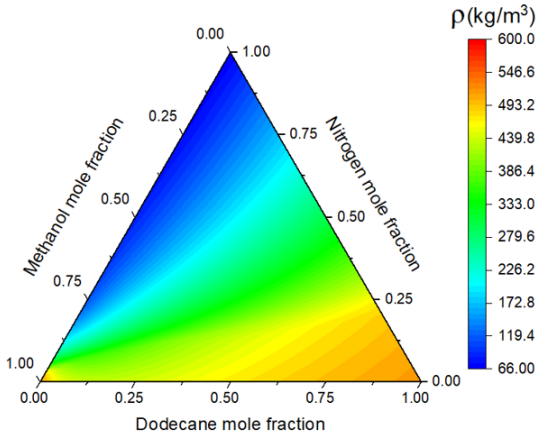

(a)

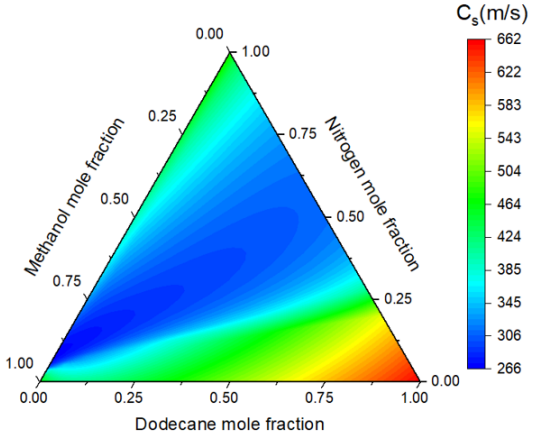

(b)

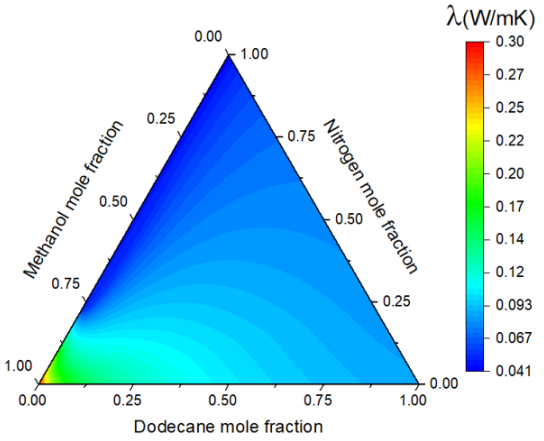

(c)

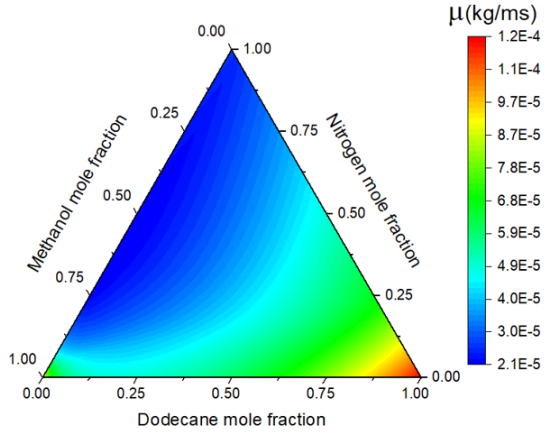

(d)

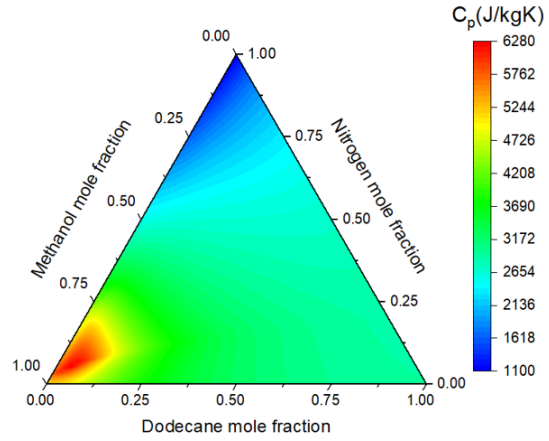

(e)

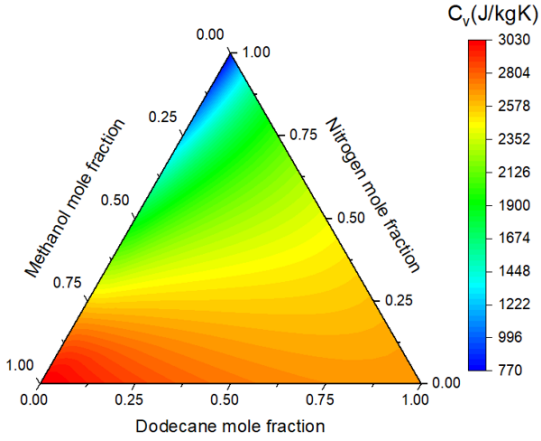

(f)

Figure A.2: Contour plots of the ternary (n-dodecane/nitrogen/methanol) mixture thermodynamic and transport properties at ($P = 106\,\text{bar}$, $T = 500\,\text{K}$). (a) density (b) sound speed (c) thermal conductivity (d) dynamic viscosity (e) isobaric heat capacity (f) isochoric heat capacity.

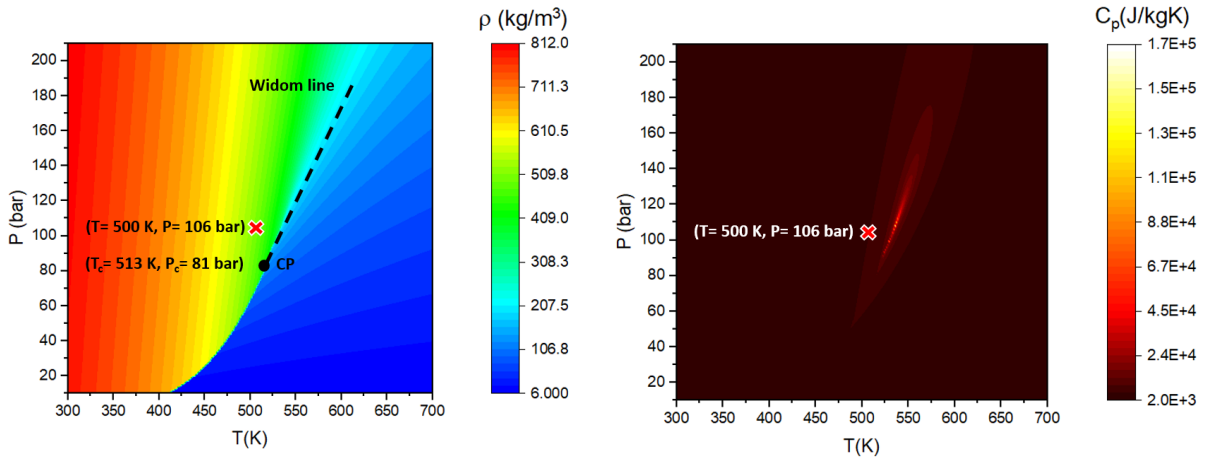

(a) (b)

Figure A.3: Pressure-temperature diagram of pure methanol (CH_3OH). (a) Density contours mapped with the widom line and the critical point (CP) (b) isobaric heat capacity contours. The red cross indicates that ($P = 106$bar and $T = 500$K) is at the vicinity of the widom line, where the isobaric heat capacity reaches a peak value.

References

[1] Engine Combustion Network (ECN), 06/01/2021. URL `https://ecn.sandia.gov/`.

[2] M. R. Baer and J. W. Nunziato. A two-phase mixture theory for the deflagration-to-detonation transition (ddt) in reactive granular materials. *International Journal of Multiphase Flow*, 12(6):861–889, 1986. ISSN 03019322. doi: 10.1016/0301-9322(86)90033-9.

[3] B. Balaji, V. Raghavan, K. Ramamurthi, and G. Gogos. A numerical study of evaporation characteristics of spherical n-dodecane droplets in high pressure nitrogen environment. *Physics of Fluids*, 23(6):063601, 2011. ISSN 1070-6631. doi: 10.1063/1.3599700.

[4] D. T. Banuti. Crossing the Widom-line – Supercritical pseudo-boiling. *The Journal of Supercritical Fluids*, 98:12–16, 2015. ISSN 08968446. doi: 10.1016/j.supflu.2014.12.019.

[5] J. Bellan. Supercritical (and subcritical) fluid behavior and modeling: Drops, streams, shear and mixing layers, jets and sprays. *Progress in Energy and Combustion Science*, 26(4-6):329–366, 2000. ISSN 03601285. doi: 10.1016/S0360-1285(00)00008-3.

[6] E. Brunner, W. Hültenschmidt, and G. Schlichthärle. Fluid mixtures at high pressures IV. Isothermal phase equilibria in binary mixtures consisting of (methanol + hydrogen or nitrogen or methane or carbon monoxide or carbon dioxide). *The Journal of Chemical Thermodynamics*, 19(3):273–291, 1987. ISSN 00219614. doi: 10.1016/0021-9614(87)90135-2.

[7] C. Chauveau, F. Halter, A. Lalonde, and I. Gokalp, editors. *An experimental study on the droplet vaporization: effects of heat conduction through the support fiber*, ILASS-EUROPE, COMO, IT, 2008.

[8] C. Chauveau, M. Birouk, F. Halter, and I. Gökalp. An analysis of the droplet support fiber effect on the evaporation process. *International Journal of Heat and Mass Transfer*, 128:885–891, 2019. ISSN 00179310. doi: 10.1016/j.ijheatmasstransfer.2018.09.029.

[9] A. Chiapolino, P. Boivin, and R. Saurel. A simple and fast phase transition relaxation solver for compressible multicomponent two-phase flows. *Computers & Fluids*, 150:31–45, 2017. ISSN 00457930. doi: 10.1016/j.compfluid.2017.03.022.

[10] T. H. Chung, M. Ajlan, L. L. Lee, and K. E. Starling. Generalized multiparameter correlation for nonpolar and polar fluid transport properties. *Industrial & Engineering Chemistry Research*, 27(4):671–679, 1988. ISSN 0888-5885. doi: 10.1021/ie00076a024.

[11] C. Crua, J. Manin, and L. M. Pickett. On the transcritical mixing of fuels at diesel engine conditions. *Fuel*, 208:535–548, 2017. ISSN 0016-2361. doi: 10.1016/j.fuel.2017.06.091.

[12] J.-C. de Hemptinne, J.-M. Ledanois, P. Mougin, and A. Barreau. *Select Thermodynamic Models for Process Simulation - A Practical Guide using a Three Steps Methodology*. Technip, 2012. ISBN 9782901638131. doi: 10.2516/ifpen/2011001.

[13] Y. Dong, O. Kaario, G. Hassan, O. Ranta, M. Larmi, and B. Johansson. High-pressure direct injection of methanol and pilot diesel: A non-premixed dual-fuel engine concept. *Fuel*, 277:117932, 2020. ISSN 0016-2361. doi: 10.1016/j.fuel.2020.117932.

[14] V. Ebrahimian and C. Habchi. Towards a predictive evaporation model for multi-component hydrocarbon droplets at all pressure conditions. *International Journal of Heat and Mass Transfer*, 54(15-16):3552–3565, 2011. ISSN 00179310. doi: 10.1016/j.ijheatmasstransfer.2011.03.031.

[15] T. García-Córdova, D. N. Justo-García, B. E. García-Flores, and F. García-Sánchez. Vapor−Liquid Equilibrium Data for the Nitrogen + Dodecane System at Temperatures from (344 to 593) K and at Pressures up to 60 MPa. *Journal of Chemical & Engineering Data*, 56(4):1555–1564, 2011. ISSN 0021-9568. doi: 10.1021/je1012372.

[16] D. Gerard and L. B. Lave. Implementing technology-forcing policies: The 1970 Clean Air Act Amendments and the introduction of advanced automotive emissions controls in the United States. *Technological Forecasting and Social Change*, 72(7):761–778, 2005. ISSN 00401625. doi: 10.1016/j.techfore.2004.08.003.

[17] H. Ghassemi, S. W. Baek, and Q. S. Khan. Experimental study on binary droplet evaporation at elevated pressures and temperatures. *Combustion Science and Technology*, 178(6):1031–1053, 2006. ISSN 0010-2202. doi: 10.1080/00102200500296697.

[18] G. Godsave. Studies of the combustion of drops in a fuel spray—the burning of single drops of fuel. *Symposium (International) on Combustion*, 4(1):818–830, 1953. ISSN 00820784. doi: 10.1016/S0082-0784(53)80107-4.

[19] Y. Gong, G. Xiao, X. Ma, K. H. Luo, S. Shuai, and H. Xu. Phase transitions of multi-component fuel droplets under sub- and supercritical conditions. *Fuel*, 287: 119516, 2021. ISSN 0016-2361. doi: 10.1016/j.fuel.2020.119516.

[20] C. Habchi. A Gibbs Energy Relaxation Model (GERM) for Cavitation Simulation. *Atomization and Sprays*, 25(4):317–334, 2015. ISSN 1044-5110. doi: 10.1615/AtomizSpr.2014010372.

[21] C. Habchi, N. Dumont, and O. Simonin. Multidimentional Simulation of Cavitating Flows in Diesel Injectors by a Homogeneous Mixture Modeling Approach. *Atomization and Sprays*, 18(2):129–162, 2008. ISSN 1044-5110. doi: 10.1615/AtomizSpr.v18.i2.20.

[22] N. Hooftman, M. Messagie, J. van Mierlo, and T. Coosemans. A review of the European passenger car regulations – Real driving emissions vs local air quality. *Renewable and Sustainable Energy Reviews*, 86:1–21, 2018. ISSN 13640321. doi: 10.1016/j.rser.2018.01.012.

[23] R. Issa. Solution of the implicitly discretised fluid flow equations by operator-splitting. *Journal of Computational Physics*, 62(1):40–65, 1986. ISSN 00219991. doi: 10.1016/0021-9991(86)90099-9.

[24] S. Jafari, H. Gaballa, C. Habchi, and J.-C. de Hemptinne. Towards Understanding the Structure of Subcritical and Transcritical Liquid–Gas Interfaces Using a Tabulated Real Fluid Modeling Approach. *Energies*, 14(18):5621, 2021. ISSN 1996-1073. doi: 10.3390/en14185621.

[25] H. Jia and G. Gogos. Investigation of liquid droplet evaporation in subcritical and supercritical gaseous environments. *Journal of Thermophysics and Heat Transfer*, 6 (4):738–745, 1992. ISSN 0887-8722. doi: 10.2514/3.11560.

[26] H. Jia and G. Gogos. High pressure droplet vaporization; effects of liquid-phase gas solubility. *International Journal of Heat and Mass Transfer*, 36(18):4419–4431, 1993. ISSN 00179310. doi: 10.1016/0017-9310(93)90126-Q.

[27] H. Jia and G. Gogos. Droplet vaporization in subcritical and supercritical environments; high vs low pressure modelling. *Acta Astronautica*, 32(2):121–129, 1994. ISSN 00945765. doi: 10.1016/0094-5765(94)90063-9.

[28] A. K. Kapila, R. Menikoff, J. B. Bdzil, S. F. Son, and D. S. Stewart. Two-phase modeling of deflagration-to-detonation transition in granular materials: Reduced equations. *Physics of Fluids*, 13(10):3002–3024, 2001. ISSN 1070-6631. doi: 10.1063/1.1398042.

[29] G. A. Karim. *Dual-fuel diesel engines*. CRC Press, 2015.

[30] R. J. Kee, M. E. Coltrin, and P. Glarborg. *Chemically reacting flow: Theory and practice*. Wiley-Interscience, Hoboken, N.J., 2003. ISBN 9780471261797.

[31] G. M. Kontogeorgis, E. C. Voutsas, I. V. Yakoumis, and D. P. Tassios. An Equation of State for Associating Fluids. *Industrial & Engineering Chemistry Research*, 35 (11):4310–4318, 1996. ISSN 0888-5885. doi: 10.1021/ie9600203.

[32] P. Koukouvinis, A. Vidal-Roncero, C. Rodriguez, M. Gavaises, and L. Pickett. High pressure/high temperature multiphase simulations of dodecane injection to nitrogen: Application on ECN Spray-A. *Fuel*, 275:117871, 2020. ISSN 0016-2361. doi: 10.1016/j.fuel.2020.117871.

[33] P. Koukouvinis, C. Rodriguez, J. Hwang, I. Karathanassis, M. Gavaises, and L. Pickett. Machine Learning and transcritical sprays: A demonstration study of their potential in ECN Spray-A. *International Journal of Engine Research*, page 146808742110202, 2021. ISSN 1468-0874. doi: 10.1177/14680874211020292.

[34] Le Ning, Q. Duan, Z. Chen, H. Kou, B. Liu, B. Yang, and K. Zeng. A comparative study on the combustion and emissions of a non-road common rail diesel engine fueled with primary alcohol fuels (methanol, ethanol, and n-butanol)/diesel dual fuel. *Fuel*, 266:117034, 2020. ISSN 0016-2361. doi: 10.1016/j.fuel.2020.117034.

[35] J. Matheis and S. Hickel. Multi-component vapor-liquid equilibrium model for LES of high-pressure fuel injection and application to ECN Spray A. *International Journal of Multiphase Flow*, 99:294–311, 2018. ISSN 03019322. doi: 10.1016/j.ijmultiphaseflow.2017.11.001.

[36] M. L. Michelsen. The isothermal flash problem. Part II. Phase-split calculation. *Fluid Phase Equilibria*, 9(1):21–40, 1982. ISSN 03783812. doi: 10.1016/0378-3812(82)85002-4.

[37] R. S. Miller, K. Harstad, and J. Bellan. Evaluation of equilibrium and non-equilibrium evaporation models for many-droplet gas-liquid flow simulations. *International Journal of Multiphase Flow*, 24(6):1025–1055, 1998. ISSN 03019322. doi: 10.1016/S0301-9322(98)00028-7.

[38] H. Nomura, Y. Ujiie, H. J. Rath, J. Sato, and M. Kono. Experimental study on high-pressure droplet evaporation using microgravity conditions. *Symposium (International) on Combustion*, 26(1):1267–1273, 1996. ISSN 00820784. doi: 10.1016/S0082-0784(96)80344-4.

[39] C. A. Passut and R. P. Danner. Correlation of Ideal Gas Enthalpy, Heat Capacity and Entropy. *Industrial & Engineering Chemistry Process Design and Development*, 11(4):543–546, 1972. ISSN 0196-4305. doi: 10.1021/i260044a016.

[40] V. B. Pedrozo, I. May, W. Guan, and H. Zhao. High efficiency ethanol-diesel dual-fuel combustion: A comparison against conventional diesel combustion from low to full engine load. *Fuel*, 230:440–451, 2018. ISSN 0016-2361. doi: 10.1016/j.fuel.2018.05.034.

[41] D.-Y. Peng and D. B. Robinson. A New Two-Constant Equation of State. *Industrial & Engineering Chemistry Fundamentals*, 15(1):59–64, 1976. ISSN 0196-4313. doi: 10.1021/i160057a011.

[42] L. Qiu and R. D. Reitz. An investigation of thermodynamic states during high-pressure fuel injection using equilibrium thermodynamics. *International Journal of Multiphase Flow*, 72:24–38, 2015. ISSN 03019322. doi: 10.1016/j.ijmultiphaseflow.2015.01.011.

[43] Richards, K.J., Senecal, P.K., and Pomraning, E. CONVERGE 3.0, Convergent Science, Madison, WI (2021).

[44] R. Saurel and R. Abgrall. A Multiphase Godunov Method for Compressible Multifluid and Multiphase Flows. *Journal of Computational Physics*, 150(2):425–467, 1999. ISSN 00219991. doi: 10.1006/jcph.1999.6187.

[45] R. Saurel, P. Boivin, and O. Le Métayer. A general formulation for cavitating, boiling and evaporating flows. *Computers & Fluids*, 128:53–64, 2016. ISSN 00457930. doi: 10.1016/j.compfluid.2016.01.004.

[46] S. S. Sazhin. Advanced models of fuel droplet heating and evaporation. *Progress in Energy and Combustion Science*, 32(2):162–214, 2006. ISSN 03601285. doi: 10.1016/j.pecs.2005.11.001.

[47] J. Schlottke and B. Weigand. Direct numerical simulation of evaporating droplets. *Journal of Computational Physics*, 227(10):5215–5237, 2008. ISSN 00219991. doi: 10.1016/j.jcp.2008.01.042.

[48] J. Schlottke, E. Dulger, and B. Weigand. A VOF-based 3D numerical investigation of evaporating, deformed droplets. *Progress in Computational Fluid Dynamics, An International Journal*, 9(6/7):426, 2009. ISSN 1468-4349. doi: 10.1504/PCFD.2009.027374.

[49] J. Seagrave, J. D. McDonald, E. Bedrick, E. S. Edgerton, A. P. Gigliotti, J. J. Jansen, L. Ke, L. P. Naeher, S. K. Seilkop, M. Zheng, and J. L. Mauderly. Lung toxicity of ambient particulate matter from southeastern U.S. sites with different contributing sources: Relationships between composition and effects. *Environmental health perspectives*, 114(9):1387–1393, 2006. ISSN 0091-6765. doi: 10.1289/ehp.9234.

[50] G. Soave. Equilibrium constants from a modified Redlich-Kwong equation of state. *Chemical Engineering Science*, 27(6):1197–1203, 1972. ISSN 00092509. doi: 10.1016/0009-2509(72)80096-4.

[51] G. Strotos, I. Malgarinos, N. Nikolopoulos, and M. Gavaises. Predicting the evaporation rate of stationary droplets with the VOF methodology for a wide range of ambient temperature conditions. *International Journal of Thermal Sciences*, 109:253–262, 2016. ISSN 12900729. doi: 10.1016/j.ijthermalsci.2016.06.022.

[52] P. Tudisco and S. Menon. Analytical framework for real-gas mixtures with phase-equilibrium thermodynamics. *The Journal of Supercritical Fluids*, 164:104929, 2020. ISSN 08968446. doi: 10.1016/j.supflu.2020.104929.

[53] C. Ware, W. Knight, and D. Wells. Memory intensive statistical algorithms for multibeam bathymetric data. *Computers & Geosciences*, 17(7):985–993, 1991. ISSN 00983004. doi: 10.1016/0098-3004(91)90093-S.

[54] L. Wei and P. Geng. A review on natural gas/diesel dual fuel combustion, emissions and performance. *Fuel Processing Technology*, 142:264–278, 2016. ISSN 03783820. doi: 10.1016/j.fuproc.2015.09.018.

[55] A. B. Wood and R. B. Lindsay. A Textbook of Sound. *Physics Today*, 9(11):37, 1956. ISSN 0031-9228. doi: 10.1063/1.3059819.

[56] G. Xiao, K. H. Luo, X. Ma, and S. Shuai. A molecular dynamics study of fuel droplet evaporation in sub- and supercritical conditions. *Proceedings of the Combustion Institute*, 37(3):3219–3227, 2019. ISSN 15407489. doi: 10.1016/j.proci.2018.09.020.

[57] S. Yang, P. Yi, and C. Habchi. Real-fluid injection modeling and LES simulation of the ECN Spray A injector using a fully compressible two-phase flow approach. *International Journal of Multiphase Flow*, 122:103145, 2020. ISSN 03019322. doi: 10.1016/j.ijmultiphaseflow.2019.103145.

[58] P. Yi, H. Zhang, and S. Yang. Evaluation of a non-equilibrium multi-component evaporation model for blended diesel/alcohol droplets. In *AIAA Scitech 2020 Forum*, Reston, Virginia, 01062020. American Institute of Aeronautics and Astronautics. ISBN 978-1-62410-595-1. doi: 10.2514/6.2020-2049.

[59] P. Yi, S. Jafari, S. Yang, and C. Habchi. Numerical analysis of subcritical evaporation and transcritical mixing of droplet using a tabulated multicomponent vapor-liquid equilibrium model. *ILASS-Europe, 29th Conference on Liquid Atomization and Spray Systems*, 2019.

[60] P. Yi, S. Yang, C. Habchi, and R. Lugo. A multicomponent real-fluid fully compressible four-equation model for two-phase flow with phase change. *Physics of Fluids*, 31 (2):026102, 2019. ISSN 1070-6631. doi: 10.1063/1.5065781.

[61] H. Zhang and S. Yang. Multi-component transcritical flow simulation using in situ adaptive tabulation of vapor-liquid equilibrium solutions. *in ILASS-Americas 31st Annual Conference on Liquid Atomization and Spray Systems*, 2021.